Solution Structure and Lipid Membrane Partitioning of VSTx1, an Inhibitor of the KvAP Potassium Channel[†,‡]

Hoi Jong Jung,[§] Ju Yeon Lee,[§] Su Hwan Kim,[§] Young-Jae Eu,[§] Song Yub Shin,[||] Mirela Milescu,[⊥] Kenton J Swartz,[⊥] and Jae Il Kim*[,§]

Department of Life Science, Gwangju Institute of Science and Technology, Gwangju 500-712, Korea, Department of Bio-Materials, Graduate School and Research Center for Proteineous Materials, Chosun University, Gwangju 501-759, Korea, and Molecular Physiology and Biophysics Section, National Institute of Neurological Disorders and Stroke, National Institutes of Health, Bethesda, Maryland 20892

Received October 28, 2004; Revised Manuscript Received February 11, 2005

ABSTRACT: VSTx1 is a voltage sensor toxin from the spider *Grammostola spatulata* that inhibits KvAP, an archeabacterial voltage-activated K^+ channel whose X-ray structure has been reported. Although the receptor for VSTx1 and the mechanism of inhibition are unknown, the sequence of the toxin is related to hanatoxin (HaTx) and SGTx, two toxins that inhibit eukaryotic voltage-activated K^+ channels by binding to voltage sensors. VSTx1 has been recently shown to interact equally well with lipid membranes that contain zwitterionic or acidic phospholipids, and it has been proposed that the toxin receptor is located within a region of the channel that is submerged in the membrane. As a first step toward understanding the inhibitory mechanism of VSTx1, we determined the three-dimensional solution structure of the toxin using NMR. Although the structure of VSTx1 is similar to HaTx and SGTx in terms of molecular fold and amphipathic character, the detailed positions of hydrophobic and surrounding charged residues in VSTx1 are very different than what is seen in the other toxins. The amphipathic character of VSTx1, notably the close apposition of basic and hydrophobic residues on one face of the toxin, raises the possibility that the toxin interacts with interfacial regions of the membrane. We reinvestigated the partitioning of VSTx1 into lipid membranes and find that VSTx1 partitioning requires negatively charged phospholipids. Intrinsic tryptophan fluorescence and acrylamide quenching experiments suggest that tryptophan residues on the hydrophobic surface of VSTx1 have a diminished exposure to water when the toxin interacts with membranes. The present results suggest that if membrane partitioning is involved in the mechanism by which VSTx1 inhibits voltage-activated K^+ channels, then binding of the toxin to the channel would likely occur at the interface between the polar headgroups and the hydrophobic phase of the membrane.

A variety of protein toxins isolated from venom of spiders, snakes, cone snails, and sea anemone interact with voltage-activated ion channels. These channels are comprised of two types of domains: a pore-forming domain constructed from the tetrameric arrangement of S5−S6 segments and four voltage-sensing domains, each constructed from the S1−S4 segments (*1*−*6*). Many toxins inhibit voltage-activated channels by targeting the external vestibule of the ion conduction pore and blocking the flow of ions (*7*−*16*). In other cases, the toxins modify gating by interacting with the voltage-sensing domains of voltage-activated channels. Examples of gating modifier toxins include the α- and *β*-scorpion toxins and sea anemone toxins that slow inactivation of Na^+ channels (*17*) and inhibitors of both voltage-activated Ca^{2+} and K^+ channels (*18*−*23*).

VSTx1 is a particularly interesting toxin that was recently isolated from the venom of the *Grammostola spatulata* tarantula and shown to inhibit KvAP (*24*, *25*), an archeabacterial voltage-activated K^+ channel whose 3D structure has been solved using X-ray crystallography (*6*). Although the receptor for VSTx1 and the mechanism of inhibition remain to be elucidated, the sequence of this toxin is similar to hanatoxin (HaTx) and SGTx, two closely related gating modifier toxins that have been shown to inhibit eukaryotic voltage-activated K^+ channels by binding to the channel's voltage sensors (*23*, *26*−*32*). It was recently reported that VSTx1 interacts with lipid membranes, leading to the proposal that the receptor for VSTx1 is located within a region of the channel that is submerged in the membrane (*30*). In a membrane access, VSTx1 is likely to interact equally well with lipid membranes containing zwitterionic (no net charge) or acidic (net negative charge) phospholipids.

[†] This study was supported by grants from the Korea Science and Engineering Foundation through the Research Center for Proteineous Materials, the Molecular and Cellular BioDiscovery Research Program, the Brain Research Center of the 21st Century Frontier Research Program (M103KV010004 03K2201 00430), the Development of Marine Novel Compounds Program of the Korean Ministry of Maritime Affairs and Fisheries, and the Intramural Research Program within the National Institute of Neurological Disorders and Stroke, National Institutes of Health. H.J.J., J.Y.L., and S.H.K. are supported in part by the Korean Ministry of Education (Brain Korea 21 program).

[‡] Atomic coordinates for the 20 converged structures of VSTx1 have been deposited in the Protein Data Bank as entry 1S6X.

* To whom correspondence should be addressed. E-mail: jikim@gist.ac.kr. Phone: +82-62-970-2494. Fax: +82-62-970-2484.

[§] Gwangju Institute of Science and Technology.

[||] Chosun University.

[⊥] National Institutes of Health.

10.1021/bi0477034 CCC: $30.25
Published on Web 03/30/2005

To better understand the inhibitory mechanism of VSTx1, in the present study we determined the three-dimensional solution structure of the toxin using NMR.[1] The close apposition of hydrophobic and basic residues evident from the VSTx1 solution structure raises the possibility that when bound to membranes the toxin would be positioned at the interface between polar headgroups and the hydrocarbon interior. Because an interfacial location for the toxin might cause the toxin−membrane interaction to be quite sensitive to the charge on the lipid headgroups, we also reexamined the partitioning of VSTx1 into lipid membranes using a spin-down assay, intrinsic tryptophan fluorescence, and fluorescence quenching by aqueous acrylamide.

MATERIALS AND METHODS

Peptide Synthesis. The amino acid sequence of VSTx1 is ECGKFMWKCKNSNDCCKDLVCSSRWKWCVLASPF (*24*). The linear precursor of VSTx1 was synthesized by solid-phase methodology of Fmoc chemistry starting from Fmoc-Phe-SAL resin using a variety of blocking groups for the protection of amino acids. The synthetic peptide was deprotected and cleaved using a mixture (82.5% TFA, 2.5% 1,2-ethanedithiol, 5% H_2O, 5% thioanisole, and 5% phenol, v/v) and then precipitated with diethyl ether. The deprotected linear peptide was diluted to a final peptide concentration of 2.5×10^{-5} M and subjected to oxidative disulfide bond formation at 4 °C for 3 days in 0.1 M ammonium acetate buffer (pH 7.8) containing 0.1 M NaCl and reduced/oxidized glutathione (molar ratio of peptide:GSH:GSSG was 1:100:10). The cyclization reaction was monitored by reversed-phase high-performance liquid chromatography (RP-HPLC), and when complete, the reaction mixture was loaded onto a CM-cellulose CM-52 column and eluted with 0.3 M ammonium acetate (pH 6.5). Preparative RP-HPLC was performed with a Shimadzu LC-6AD system and Shimadzu LC-10Avp system with an ODS column (20 × 250 mm). The structure and purity of the synthetic peptide were confirmed by analytical RP-HPLC and MALDI-TOF mass spectrometry. The chromatographic behavior of synthetic VSTx1 was compared to native VSTx1 (Figure 1) using a Beckman analytical gradient RP-HPLC and an ODS column (20 × 250 mm). Toxins were eluted with a linear gradient from 25% mobile phase B (24.9% acetonitrile in water, 0.1% trifluoroacetic acid) to 65% mobile phase B over 40 min at a flow rate of 1 mL/min.

NMR Spectroscopy. For NMR experiments, the final peptide concentration was 10 mM at pH 3.5 in water containing 10% (v/v) ^2H_2O. NMR experiments were carried out at 283 and 300 K on a Bruker DRX 600 spectrometer. TOCSY spectra were recorded using a MLEV-17 pulse scheme (*33*) with isotropic mixing times of 80 ms. NOESY spectra were recorded with mixing times of 80, 150, and 250 ms. The two-dimensional NMR experiments included TOCSY and NOESY experiments and were carried out using the WATERGATE scheme for water suppression (*34*). DQF-COSY (*35*) and PE-COSY (*36*) were recorded to obtain the constraints for the torsion angles and stereospecific assignments, respectively. For the amide proton exchange experiments, the lyophilized sample was dissolved in ^2H_2O, and then a series of TOCSY experiments were performed at 300 K (*33*). Processing and analysis of the spectra were done using XWIN NMR and ANSIG programs.

Structure Calculations. Quantitative determination of cross-peak intensities was based on the counting levels. Observed NOE data were classified into four distance ranges, 1.8−2.7, 1.8−3.5, 1.8−5.0, and 1.8−6.0 Å, corresponding to strong, medium, weak, and very weak NOE values, respectively. Pseudoatoms were used for the methyl protons or the nonstereospecifically assigned methylene protons (*37*). Correcting factors for the use of pseudoatoms were added to the distance constraints (*38*). The backbone NH−C^{α}H coupling constants were estimated from the DQF-COSY spectrum and were converted to backbone torsion angle ϕ constraints according to the following rules. For $^3J_{NH-C\alpha H}$ values of <5.5 Hz, the ϕ angle was constrained in the range of $-65 \pm 25°$; for $^3J_{NH-C\alpha H}$ values of >8.0 Hz, it was constrained in the range of $-120 \pm 40°$ (*39*, *40*). The range of the χ^1 side chain torsion angle constraints and the stereospecific assignment of the prochiral β-methylene protons were obtained using the $^3J_{\alpha\beta}$ coupling constants combined with the intraresidue NH−C^{β}H NOEs (*41*). The $^3J_{\alpha\beta}$ coupling constants were determined from the E-COSY spectrum in ^2H_2O. For the t^2g^3, g^2g^3, and g^2t^3 conformations around the $C^{\alpha}-C^{\beta}$ bonds, the χ^1 side chain torsion was constrained in the ranges of $-60 \pm 30°$, $60 \pm 30°$, and $180 \pm 30°$, respectively (*42*). The hydrogen bond acceptors for the slowly exchanged amide protons were identified by analyzing the preliminary calculated structures (*10*, *43*). The distance restraints of hydrogen bonds were added as target values of 1.8−2.3 Å for NH(*i*)−O(*j*) bonds and 2.8−3.3 Å for N(*i*)−O(*j*) bonds. The disulfide bonding pattern of VSTx1 was determined during the structural determination process. On the basis of the strategy proposed by Nilges (*44*), ambiguous distance restraints of disulfide pairing were introduced in the initial run of the structural calculation. With this initial calculation, the disulfide pairing of Cys2−Cys16 was unambiguously determined. Analyzing the predetermined structure of VSTx1, two types of disulfide pairing were possible (Cys9−Cys21, Cys15−Cys28 and Cys9−Cys28, Cys15−Cys21). Therefore, we performed two sets of structure calculation with each of the two disulfide bonding patterns. By comparing the averaged total X-PLOR energy of the two sets of calculations in the final refinement, we determined the specific disulfide bonding pattern (Cys2−Cys16, Cys9−Cys21, and Cys15−Cys28). The total X-PLOR energy of this type of disulfide bonding pattern was more stable than the others. The 20 best structures based on the X-PLOR energy were chosen for structural analysis. The structures were analyzed using the PROCHECK_NMR (*45*). Structural figures were generated using the MOLMOL program (*46*). All calculations were carried out by using the dynamical simulated annealing protocols in the X-PLOR 3.851 program (*47*).

Spin-Down Assay. The interaction of VSTx1 with large unilamellar vesicles (LUVs) was initially evaluated by

[1] Abbreviations: DQF-COSY, double-quantum-filtered correlation spectroscopy; Fmoc, 9-fluorenylmethoxycarbonyl; MALDI-TOF mass, matrix-assisted laser desorption/ionization time-of-flight mass spectrometry; NOE, nuclear Overhauser effect; NOESY, NOE spectroscopy; NMR, nuclear magnetic resonance; PE-COSY, primitive exclusive correlation spectroscopy; PDB, Protein Data Bank; RMS, root mean square; RP-HPLC, reversed-phase high-performance liquid chromatography; TFA, trifluoroacetic acid; TOCSY, total correlation spectroscopy.

incubating aqueous solutions of the toxin (10 μM) with varying amounts of vesicles for 1 h at room temperature, centrifuging the vesicles (1 h, 100000*g*), and determining the toxin concentration remaining in the aqueous phase. LUVs were prepared by drying lipids (POPG and/or POPC, 25 mg/mL) under nitrogen gas, washing the lipid pellet with pentane, and resuspension by vortexing for 1 h in an aqueous buffer containing 10 mM Tris, pH 7.4, 0.1 mM EDTA, and 150 mM NaCl. For POPC vesicles 50 mM NaCl was substituted for 150 mM NaCl. Vesicles were extruded 20 times using 0.1 μm polycarbonate filters (Avanti Polar Lipids, Inc.). Aqueous concentrations of VSTx1 (following separation of vesicles by centrifugation) were determined using RP-HPLC (Figure 5) with an ODS (C-18) column (4.6 $\times$ 250 mm; 5 μm, 90 Å). Toxin was eluted with a linear gradient of 20−60% mobile phase B over 20 min at 1 mL/min where mobile phase A was 0.1% TFA in water and mobile phase B was 0.08% TFA in acetonitrile.

Tryptophan Fluorescence and Tryptophan Quenching. The effect of membrane partitioning (using small unilamellar vesicles) on the fluorescence emission spectrum for tryptophans in VSTx1 (3.0 μM) was examined as previously described (*48*). Quenching of tryptophan fluorescence by the titration of 0.4 M acrylamide in the presence of lipid vesicles was examined using a peptide:lipid molar ratio of 1:200 (3.0 μM VSTx1 and 600 μM phospholipid vesicles). Changes in fluorescence were plotted according to the Stern−Volmer equation $F_0/F = 1 + K_{sv}[Q]$, where F_0 is the fluorescence of the peptide in the absence of acrylamide, F is the fluorescence of the peptide in the presence of acrylamide, K_{sv} is the Stern−Volmer quenching constant, and [Q] is the concentration of acrylamide.

RESULTS

Synthesis of VSTx1. A linear precursor of VSTx1 was synthesized using solid-phase methodology and Fmoc chemistry. Controlled air oxidation of a linear precursor yielded satisfactory amounts of a correctly folded oxidized compound on RP-HPLC. The MALDI-TOF analysis of synthetic VSTx1 showed the expected molecular mass (3997.7 Da) and that the synthetic toxin coeluted with the native toxin purified from *G. spatulata* venom (Figure 1).

NMR Analysis. Sequence-specific resonance assignments were established according to the standard protocol, based on a set of traditional two-dimensional experiments (*49*). Identification of the amino acid spin system was based on scalar coupling patterns observed in DQF-COSY and TOCSY experiments, complemented by the results of NOESY measurements. The identified spin system was ordered along the primary structure of VSTx1 through interresidue sequential NOEs observed on the NOESY spectrum. The pattern of observed NOEs was ultimately interpreted in terms of the secondary structure of the molecule. As summarized in Figure 2, VSTx1 contains two β-strands consisting of residues 19−22 and 27−30, which are arranged in an antiparallel fashion, and several turns. This was based on large $^3J_{HN\alpha}$ coupling constants (Lys19, Val20, and Val29), strong sequential $d_{\alpha N}$, interstrand NH−NH and NH−C$^\alpha$H connectivities, and slowly exchanging amide protons (Leu19, Val20, Ser22, Trp27, Cys28, Val29, and Leu30) that give a discrimination of the β-sheet.

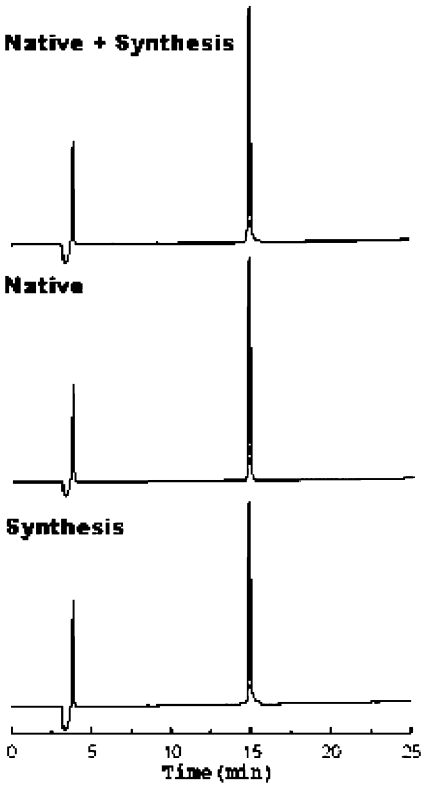

FIGURE 1: Comparison of the chromatographic behavior of synthetic VSTx1 and native VSTx1. RP-HPLC chromatograms for synthetic VSTx1 and native VSTx1 injected either separately or together.

Calculation of the Solution Structure of VSTx1. For the structure calculations of VSTx1, we used 721 distance constraints derived from the interproton NOE cross-peaks, 18 dihedral angle constraints from the coupling constraints, 8 hydrogen bond constraints from the hydrogen−deuterium exchange-out experiments, and 9 disulfide bond constraints, giving a total of 756 constraints. The 8 distance constraints related to hydrogen bonds are as follows: Trp7(CO)−Cys28(HN), Val20(CO)−Val29(HN), Ser22(HN)−Trp27(CO), and Ser22(CO)−Trp27(HN). VSTx1 contains six cysteine residues, but no information on the disulfide connectivities of the toxin was available. We therefore determined the disulfide pairing using the "ambiguous distance restraints procedure" proposed by Nilges (*44*). Using this protocol, the three disulfide bonds of VSTx1 were determined to be Cys2−Cys16, Cys9−Cys21, and Cys15−Cys28. We carried out the simulated annealing calculations starting from 100 initial random VSTx1 structures and selected 20 final structures that were in good agreement with the NMR experimental constraints, for which the NOE distance and torsion angle violations were smaller than 0.3 Å and 3°, respectively. The evaluated structural statistics for these 20 converged structures are summarized in Table 1. The low values of the Lennard-Jones van der Waals energy and the small deviations from the idealized covalent geometry indicate the absence of serious bad contact and distortion in the converged structures. Except for the N-terminal residue (Glu1) and the C-terminal segment (residues Ala31 to Phe34), the average pairwise RMS deviation between the 20 individual structures was 0.44 Å for the backbone atoms and 1.08 Å for all heavy atoms. Figure 3 shows the atomic RMS deviations and the angular order parameters for ϕ and

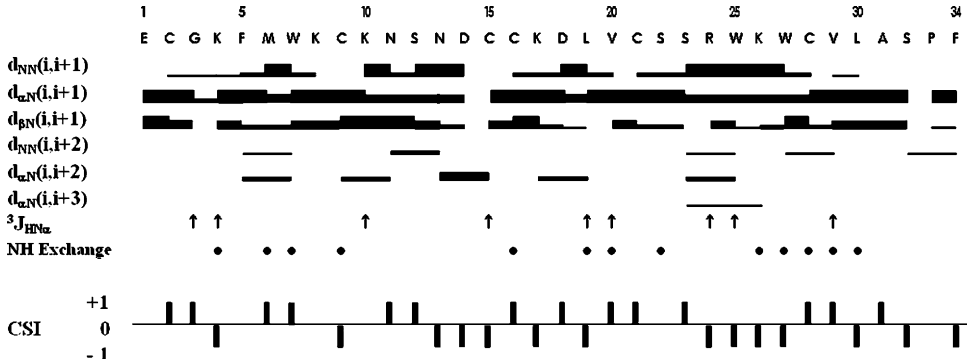

FIGURE 2: Summary of the sequential NOE connectivities, $^3J_{HN\alpha}$ coupling constants, and slowly exchanging backbone NH protons observed in VSTx1. The NOEs are classified into strong, medium, weak, and very weak, according to the height of the filled bars. The values of the $^3J_{HN\alpha}$ coupling constants are indicated by ↑ (>8 Hz) and ↓ (<5.5 Hz) symbols. The chemical shift index (CSI) is indicated by a ternary index with values of −1, 0, and +1. The values of −1 and +1 indicated a shift deviation from the random coil value of >0.1 ppm upfield and downfield, respectively; those within the range of the random coil value are given a value of 0.

Table 1: Structural Statistics for the 20 Lowest Energy Structures

RMSD from exptl distance restraints (Å)[a] (721)	0.022 ± 0.0003
RMSD from exptl dihedral angle restraints (deg)[a] (18)	0.352 ± 0.030
energetic statistics (kcal/mol)[b]	
F_{NOE}	16.95 ± 0.496
F_{tot}	0.146 ± 0.026
F_{repul}	9.385 ± 0.479
E_{LJ}	−79.515 ± 2.174
RMSD from idealized geometry	
bonds (Å)	0.003 ± 0.00004
angles (deg)	0.556 ± 0.003
impropers (deg)	0.420 ± 0.003
Ramanchandran analysis (residues 2−30)[c]	
most favored (%)	60.0
additional allowed (%)	31.8
generously allowed (%)	8.2
disallowed region (%)	0.0
average pairwise RMS difference (Å)[c]	
backbone (residues 2−30)	0.44 ± 0.11
all heavy atoms (residues 2−30)	1.08 ± 0.12

[a] The number of each experimental constraint used in the calculations is given in parentheses. [b] F_{NOE}, F_{tot}, and F_{repul} are energies related to the NOE violations, torsion angle violations, and van der Waals repulsion term, respectively. The values of the force constants used for these terms are the standard values as depicted in the X-PLOR 3.1 manual. E_{LJ} is the Lennard-Jones van der Waals energy calculated with the CHARMM empirical energy function, which was not included in the simulated annealing calculation. [c] The program PROCHECK_NMR was used to assess the stereochemical quality of the structures.

ψ torsion angles as a function of the residue number. Except for the N-terminal residue (Glu1) and the C-terminal segment (residues Ala31 to Phe34), the structure of the backbone from Cys2 to Leu30 is well defined. The angular order parameters for most residues in this region also show high S values (>0.95) and the backbone RMS deviation is less than 0.5, indicating that they are well defined (Figure 3). However, the atomic RMS deviation of all heavy atoms for each of Lys4, Lys8, Lys10, Asn13, Asp14, Lys17, Arg24, and Leu30 is greater than 1.3 Å. These residues, except for Asn13 and Leu30, have polar or charged side chains and exist at the surface of the molecules. The C-terminal segment showed some apparent deviations from the sterically allowed (ϕ and ψ) limits, which reflects the randomness of the conformationally disordered backbone in the segments. This may be the result of a lack of medium- and long-range NOE constraints due to the inherent flexibility of both segments.

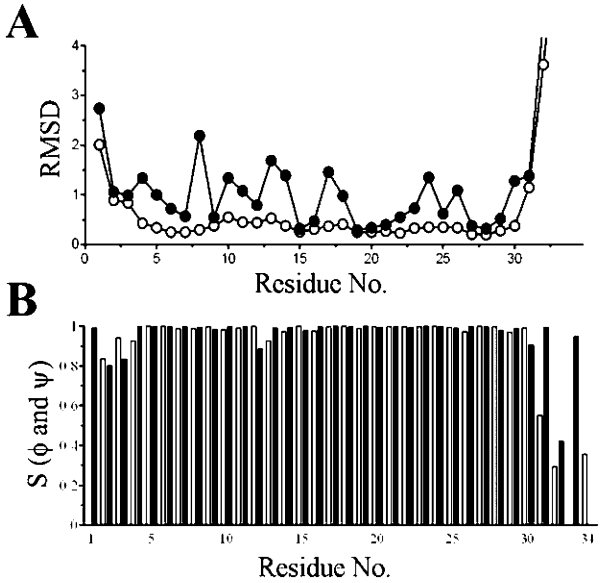

FIGURE 3: (A) Distribution of the RMSDs of backbone atoms (○) and all heavy atoms (●) for the 20 converged structures. (B) Angular order parameters for ϕ (□) and ψ (■) angles calculated from the 20 converged structures. The S values define the two limits of an exactly defined angle ($S = 1$) and a completely random distribution of the angle ($S = 0$).

Figure 4 shows the best-fit superposition of the 20 converged structures.

Molecular Structures of VSTx1. Figure 4 shows that VSTx1 is composed of two β-strands, strand I (Leu19 to Ser22) and strand II (Trp27 to Leu30), connected by several chain reversals. The first is a type II β-turn (Lys4 to Trp7). The second reversal occurs at residues Cys9−Ser12 (a type IV β-turn, miscellaneous type) and is well defined but not stabilized by hydrogen bonds. The third reversal (Cys16−Leu19) is a type II β-turn in which the average dihedral angles for Lys17 and Asp18 are $\psi_2 = 150.2°$, $\phi_3 = 57.8°$, and $\psi_3 = 19.5°$, respectively. In this turn, Cys16 is hydrogen-bonded to the Leu19, and slow H−^{2}H exchange rates of Cys16 and Leu19 are observed in the H−^{2}H exchange experiment. The final reversal occurs at residues Ser23−Lys26 and forms a β-hairpin turn (a type I β-turn) with $\psi_2 = -43.2°$ and $\phi_3 = -88.7°$.

Surface Profile of VSTx1. On the surface of VSTx1 there are six positively charged residues (Lys4, Lys8, Lys10, Lys17, Arg24, and Lys26), three negatively charged residues

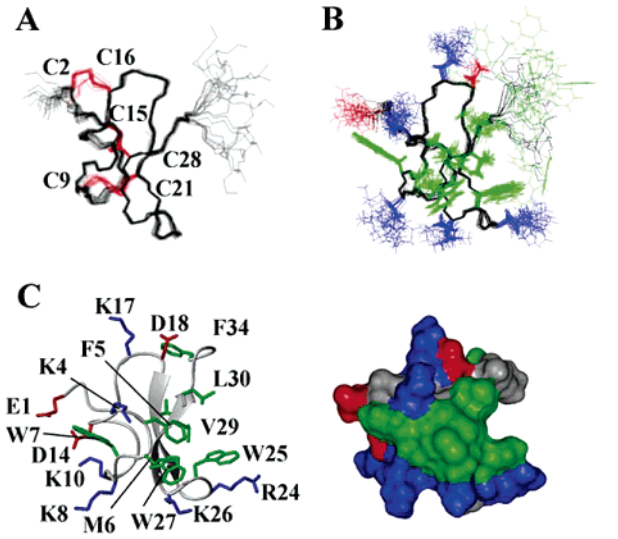

FIGURE 4: The best-fit superposition of the backbone atoms (N, C^{α}, and C) (A) and heavy atoms (B) for the 20 converged structures. (C) The surface hydrophobic patches and some charged residues in VSTx1. Hydrophobic residues are colored green, and basic and acidic residues are colored blue and red, respectively. The structure topology of the double-stranded antiparallel β-sheet was identified by MOLMOL.

(Glu1, Asp14, and Asp18), and 10 hydrophobic residues (Phe5, Met6, Trp7, Leu19, Val20, Trp25, Trp27, Val29, Leu30, and Phe34) that are highly exposed to the solvent. Most of these highly exposed hydrophobic residues (Phe5, Met6, Leu19, Val20, Trp25, Trp27, Val29, and Leu30) comprise one surface of the structure. The orientations of the phenyl ring of Phe5 and the indole rings of Trp25 and Trp27 are well determined (χ^1 angular order parameters of Phe5, Trp25, and Trp27 are 0.995, 0.996, and 1.0, respectively), and Met6 is sandwiched between the phenyl ring of Phe5 and the indole ring of Trp27. In the NMR spectra, the α-proton of Met6 was observed at unusually upfield positions (2.99 ppm) due to a ring current shift produced by Phe5. The indole ring of Trp7 that protrudes to the side of the hydrophobic patch is also well fixed (χ^1 angular order parameters of 0.998) and produces a chemical shift of the NH and $C^{\beta}H$ of the Lys4 residue to unusual positions (5.204 and 0.494 ppm, respectively). Of the eight charged residues, four basic residues (Lys4, Lys8, Arg24, and Lys26) immediately surround the hydrophobic patch on the surface of the toxin.

Interaction of VSTx1 with Lipid Membranes. In a previous study, VSTx1 was observed to interact with lipid vesicles containing either the acidic phospholipid 1-palmitoyl-2-oleoyl-*sn*-glycero-3-phosphoglycerol (POPG) or the zwitterionic (neutral) phospholipid 1-palmitoyl-2-oleoyl-*sn*-glycero-3-phosphocholine (POPC) (*30*). Membrane partitioning of VSTx1 is not surprising given the size of the hydrophobic patch evident from the structure of the toxin (Figure 4). However, the positioning of many basic residues near the hydrophobic patch suggests that the toxin could not freely diffuse into the hydrophobic phase of the membrane, but would be positioned near the polar headgroup region of the membrane. In particular, interactions between the abundant basic residues on the toxin surface and acidic headgroups on lipids would be expected to enhance partitioning. We therefore reexamined the interaction between VSTx1 and membranes, initially using a spin-down assay. Aqueous solutions of the VSTx1 were incubated with lipid vesicles for 1 h, after which time vesicles were centrifuged and the concentration of toxin was measured in the aqueous supernatant. POPG vesicles were very effective at reducing the concentration of the toxin in the aqueous phase (Figure 5A,B), suggesting that the toxin binds to acidic vesicles. However, in contrast to previous results (*30*), zwitterionic vesicles were unable to lower the concentration of VSTx (Figure 5C). The mole fraction partition coefficient (K_x) (*50*) determined for POPG vesicles was 1.1×10^5 (Figure 5D), consistent with previous results (*30*), but the K_x estimated for POPC is $<10^2$.

We next examined the effects of lipid vesicles on tryptophan fluorescence since three tryptophan residues are located on the hydrophobic surface of the toxin and hydrophobic environments are well known to produce a blue shift of the emissions spectra for tryptophan (*51*). In the same buffer used for the spin-down assay VSTx1 displayed fluorescence emission maxima around 350 nm (Figure 6A, black trace), typical for tryptophan in polar surroundings, suggesting that the three tryptophan residues in VSTx1 are located in a hydrophilic environment. This result is consistent with the NMR structure of the toxin where all three tryptophan residues exhibit extensive solvent exposure. When aqueous solutions of VSTx1 were incubated with phospholipid vesicles containing either POPG or a 1:1 mix of POPG and POPC, we observed a significant blue shift in the fluorescence emission spectrum of the toxin (Figure 6A, red and green traces, respectively). The vesicle-induced shift of the emission maxima for VSTx1 was not observed for vesicles containing POPC (Figure 6A, blue trace), consistent with the spin-down assay and suggesting that the toxin does not interact with zwitterionic vesicles. In contrast to our results with VSTx1, we observed blue shifts following the addition of either POPG or POPC to aqueous solutions of melittin (Figure 6A) (*52*). The blue shift observed for melittin was significantly larger than for VSTx1, suggesting that the way these proteins interact with the membrane is distinct. Taken together, these results suggest that VSTx1 interacts rather selectively with acidic phospholipid vesicles and some of the tryptophan residues are exposed to a hydrophobic environment when the toxin binds to membranes.

We next asked whether the interaction of VSTx1 with membranes alters the accessibility of the toxin's tryptophan residues to acrylamide, an aqueous quencher of tryptophan fluorescence. Stern−Volmer plots for the quenching of tryptophan fluorescence by acrylamide were constructed for VSTx1 and melittin in the presence of phospholipid vesicles containing POPG, POPC, or a 1:1 mix of the two lipids (Figure 6B). The fluorescence intensity of melittin decreased in a concentration-dependent manner following the addition of acrylamide, a result that was similar in the presence of all three vesicle compositions (Figure 6B and data not shown). VSTx1 fluorescence was also quenched by acrylamide in the presence of vesicles containing POPG, but in these instances the amount of quenching was somewhat greater than for melittin. In contrast, the degree of quenching by acrylamide was much greater for VSTx1 in the presence of POPC vesicles when compared to POPG vesicles (Figure 6B) and, in this instance, was no different than what was observed in the absence of lipids (not shown). These results demonstrate that the interaction of VSTx1 with acidic

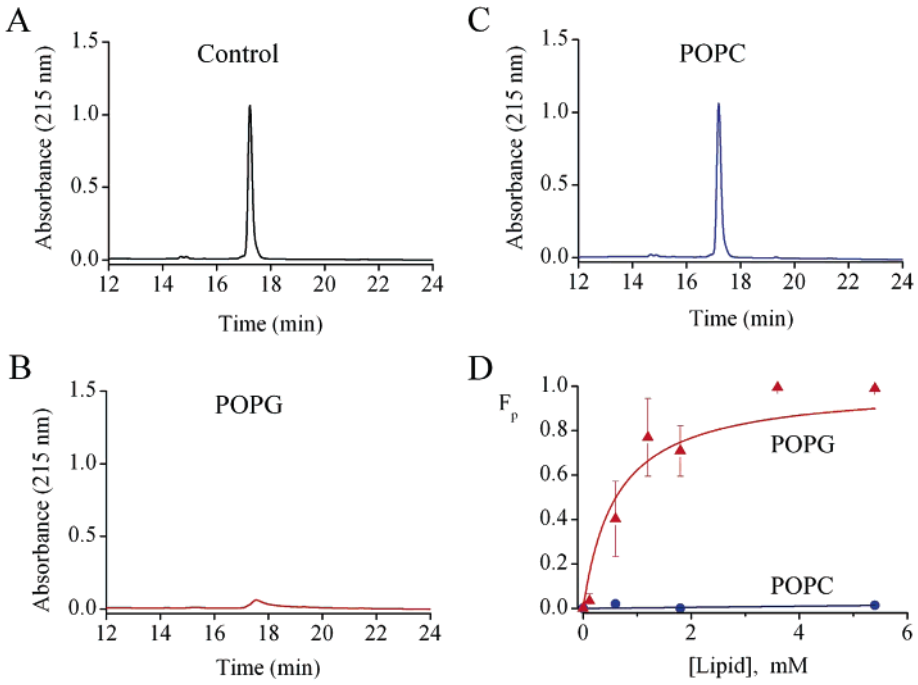

FIGURE 5: Interaction of VSTx1 with lipid vesicles. Reversed-phase HPLC profiles of VSTx1 present in the supernatant after ultracentrifugation to pellet vesicles in the absence (A) or after addition of 3 mM POPG vesicles (B) or 3 mM POPC vesicles (C). (D) Fraction of VSTx1 partitioned into vesicles (F_p) plotted as a function of available lipid concentration (60% of total lipids). Data points are the mean ± SEM ($n = 3$). Smooth curves were generated by fitting the following equation to the data: $F_p = (K_x[\text{lipid}])/(K_x[\text{lipid}] + 55.3)$.

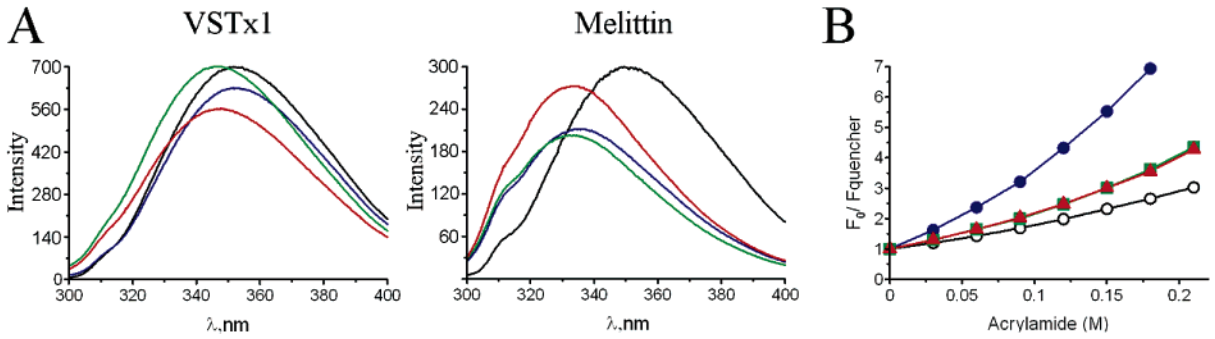

FIGURE 6: Membrane interaction of VSTx1. (A) Changes of VSTx1 and melittin in Trp fluorescence in POPC (blue), POPC:POPG (1:1) (green), and POPG (red) membranes. (B) Stern−Volmer plots for the quenching of Trp fluorescence of VSTx1 (●, ■, and ▲) and melittin (○) by an aqueous quencher, acrylamide, in the presence of POPC (blue), POPC:POPG (1:1) (green), and POPG (red) membranes. Melittin gives almost the same result for all membrane compositions.

phospholipid vesicles is accompanied by a decrease in the aqueous accessibility of tryptophan residues on the hydrophobic surface of the toxin.

DISCUSSION

Structural Comparison between VSTx1 and Other Toxins. Figure 7 shows the primary and tertiary structure of VSTx1 along with GsMTx-4, HaTx, and SGTx. VSTx1 inhibits the KvAP potassium channel through an unknown mechanism (*24*) but has been shown to partition into membranes (*30*). GsMTx-4 inhibits mechanosensitive channels by perturbing the mechanical properties of the lipid bilayer (*53*, *54*). Both HaTx and SGTx inhibit voltage-activated K^+ channels by interacting with the voltage sensors and stabilizing a resting/closed conformation (*23*, *26*−*29*, *31*, *32*). All of these toxins have the same disulfide connectivity, Cys (I−IV), Cys (II−V), and Cys (III−VI), which comprises a cystine knot motif that appears to be a highly efficient motif for structure stabilization. These toxins also share a common structural feature in that one face is almost exclusively hydrophobic, which has been shown to be an important determinant of SGTx binding to Kv2.1 channels (*32*). Despite these similarities, none of the most critical residues in SGTx and HaTx are well conserved in VSTx1. Alanine substitutions at six positions (Arg3, Arg22, Trp30, Leu5, Phe6, and Asp24) in SGTx have been shown to greatly weaken interactions with the Kv2.1 channel, with K_d values >150-fold (perturbation energy $|\Delta\Delta G|$ values > 3 kcal mol^{-1}) higher than the wild-type SGTx (*32*). From their solution structures we can see that Trp30 of HaTx and SGTx is replaced by Leu30 in VSTx1. Leu5 and Phe6 of HaTx and SGTx are replaced by Phe5 and Trp27 of VSTx1. In the case of the important polar residues, Arg3 in HaTx and SGTx is replaced by Trp7 in VSTx1, and Lys/Arg22 in HaTx and SGTx is a serine in VSTx1. One of basic residues of VSTx1, Lys4, is located at the same position with Tyr4 in HaTx and SGTx, which in the case of SGTx results in a moderate perturbation ($|\Delta\Delta G| = 1.2$ kcal mol^{-1}) when mutated to alanine (*32*). The side chain of Lys4 in VSTx1 projects in the same direction as the residues in the hydrophobic patch, an arrangement that

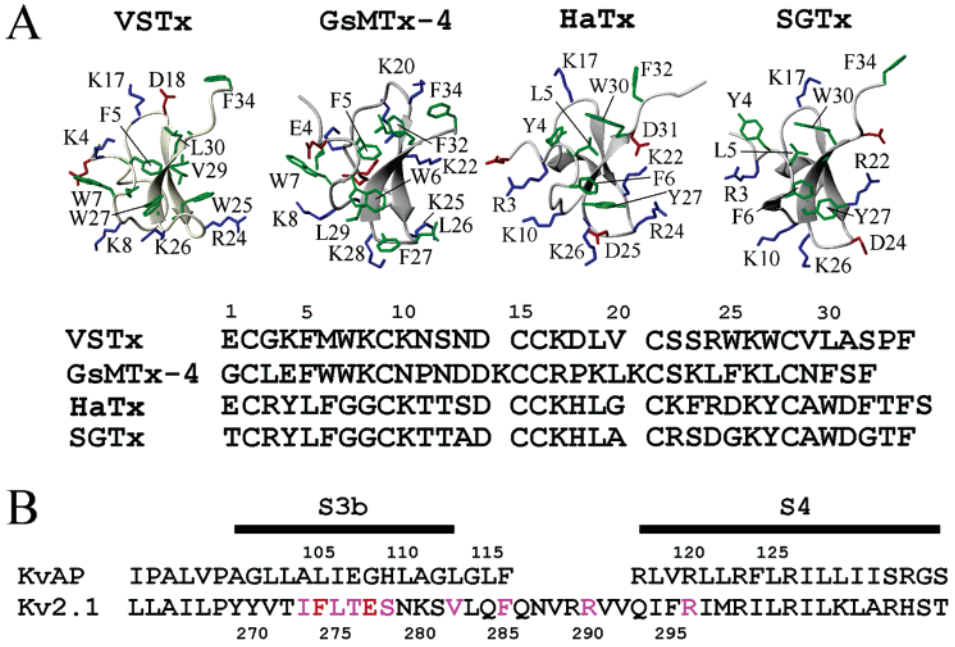

FIGURE 7: (A) Comparison of the distribution of the hydrophobic residues and charged residues on the surfaces of VSTx1, GsMTx-4, HaTx, and SGTx. Hydrophobic residues are colored green, and basic and acidic residues are colored blue and red, respectively. The coordinates of GsMTx-4, HaTx, and SGTx were obtained from PDB entries 1LU8, 1D1H, and 1LA4, respectively. Amino acid sequences of VSTx1, GsMTx-4, HaTx, and SGTx are illustrated at the bottom. (B) Sequence alignment between KvAP and Kv2.1 in the region of the voltage-sensing domain. Pink and red residues in Kv2.1 are positions where mutations produce changes in HaTx binding that are moderate or large, respectively.

is supported by NMR spectra in which the side chain of Lys4 is well fixed (χ^1 angular order parameters of 0.998) and the $C^\beta H$ chemical shift of the Lys4 backbone is moved to a upfield position (0.494 ppm) by the indole ring of Trp7. In VSTx1, Lys8, Arg24, and Lys26 are similarly positioned adjacent to the hydrophobic patch. This stands in contrast to HaTx and SGTx where the hydrophobic patch protrudes away from the level of the surrounding basic residues (Figure 8).

Of the toxins discussed thus far, VSTx1 seems to most closely resemble GsMTx-4, an inhibitor of mechanosensitive channels (*53*). When we compare the hydrophobic and charged residues between the two toxins, the hydrophobic residues Trp7, Phe5, and Trp27 of VSTx1 are identical to Trp7, Phe5, and Trp6 of GsMTx-4 (Figure 7). The direction of the acidic residue Glu4 in GsMTx-4 is also toward the hydrophobic patch, similar to Lys4 of VSTx1, and the $C^\beta H$ is shifted to an upfield position (0.152 and 0.169 ppm) by the indole ring of Trp7. Although the positions of other basic residues in VSTx1 are rather similar when compared to GsMTx-4, Lys25 and Lys28 of the fourth reverse turn of GsMTx-4 are directed away from the hydrophobic patch, opposite to the corresponding residues (Arg24 and Lys26) of VSTx1 (Figures 7 and 8).

Membrane Partitioning. Both VSTx1 and GsMTx-4 have been shown to partition into lipid membranes (*30*, *54*). We also found that VSTx1 interacts with acidic POPG vesicles with a K_x value of 1.1×10^5, in excellent agreement with that of Lee and MacKinnon (*30*). However, our results also show that the interaction of VSTx1 with membranes requires acidic phospholipids, whereas the previous study suggested that VSTx1 interacts equally well with acidic and zwitterionic phospholipid vesicles. We verified this result using three assays (spin down, blue shift in tryptophan fluorescence, acrylamide quenching), and in each instance we observed no evidence of VSTx1 partitioning for zwitterionic vesicles. Our results are quite consistent with what would be predicted from the structure of the toxin alone. Indeed, it was the toxin structure that motivated us to reassess the lipid charge dependence for partitioning. The large hydrophobic patch on VSTx1 is intimately surrounded by many basic residues, which should prevent the hydrophobic patch of the toxin from interacting with the hydrophobic phase of neutral zwitterionic POPC membranes. In contrast, one can readily see how the favorable interactions between basic residues on the toxin and acidic phospholipids, which are known to be crucial for many other proteins that interact with membranes (*55*), could critically support membrane interactions for VSTx1. The structure of VSTx1, together with the dependence of membrane interactions on phospholipid charge, suggests that the toxin is positioned at the interface between polar headgroups and the hydrophobic phase of the membrane.

Mechanisms of Channel Inhibition. There is considerable evidence that HaTx and SGTx interact with the S3b helix within the voltage sensor of voltage-activated K^+ channels and inhibit activation of the channel by stabilizing a resting conformation of the voltage sensors (*23*, *26*−*29*, *31*). Where does VSTx1 bind to KvAP and what is the mechanism by which the toxin inhibits the channel? Although the receptor for VSTx1 within the KvAP channel has yet to be identified, Ruta and MacKinnon have argued that the toxin interacts with the voltage-sensing domains (*24*, *56*). Interestingly, the residues in the Kv2.1 channel where mutations have either moderate or large effects on HaTx binding (*28*, *29*) (colored pink and red, respectively, in Figure 7) are not conserved in KvAP, suggesting that at least the details of the toxin−channel interaction are different between HaTx and VSTx1. There are also important functional differences between the two toxins. Unlike the case with HaTx where toxin-bound

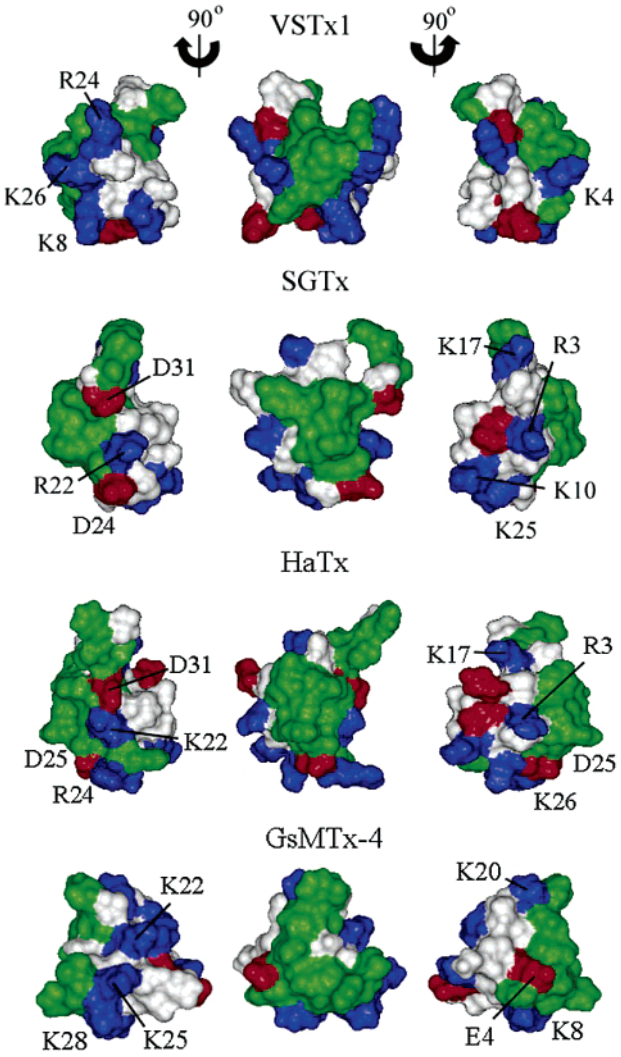

FIGURE 8: Surface profiles of VSTx1, SGTx, HaTx, and GsMTx-4. The right and left structures are 90° rotations about the vertical axis relative to the center structures. Hydrophobic residues are colored green, and some interesting basic and acidic residues are colored blue and red, respectively. The other residues are colored white.

channels can open with strong depolarization of the membrane (*31*), the inhibitory effect of VSTx1 cannot be overcome by membrane depolarization to voltages as positive as +100 mV (*24*). In addition, it has been suggested that binding of VSTx1 requires depolarization of the membrane (*25*), whereas in the case of HaTx and SGTx binding occurs when the membrane is constantly held at −100 mV (*31*). One possible explanation for these observations is that VSTx1 interacts with activated voltage sensors, whereas HaTx and SGTx interact with resting voltage sensors. If HaTx and SGTx act to retard activation of the channel, why does VSTx1 not enhance activation? Although this question remains unanswered, it has been proposed that the channel inactivates once the voltage sensors are stabilized in an activated conformation (*25*). The structures of these toxins might provide an explanation for why these two types of toxins have such different effects on their target channels. As discussed above, the hydrophobic face of VSTx1 is intimately surrounded by basic residues (Figures 7 and 8), and there is a strong dependence of membrane partitioning on acidic phospholipids (Figures 5 and 6), both of which suggest that the toxin would be confined to the interface between polar headgroups and the hydrophobic portion of the membrane. Although HaTx and SGTx exhibit very similar membrane partitioning (data not shown) and contain a hydrophobic cluster of residues that is surrounded by basic residues (Figures 7 and 8), in these cases the hydrophobic residues form a patch that protrudes about 8 Å from the level of the surrounding polar residues. In addition, the hydrophobic face of VSTx1 contains three tryptophan residues (Trp7, Trp25, Trp27), whereas the equivalent face of HaTx and SGTx only contain one, indicating that the hydrophobic face of VSTx1 is considerably more polar and favoring of an interfacial environment than the equivalent region of the other toxins. Thus, the hydrophobic protrusions on HaTx and SGTx might dip into the hydrophobic portion of the membrane somewhat further than VSTx1 even though all of these toxins are probably located near the interface.

REFERENCES

1. Kubo, Y., Baldwin, T. J., Jan, Y. N., and Jan, L. Y. (1993) Primary structure and functional expression of a mouse inward rectifier potassium channel, *Nature 362*, 127−133.
2. Doyle, D. A., Cabral, J. M., Pfuetzner, R. A., Kuo, A., Gulbis, J. M., Cohen, S. L., Chait, B. T., and Mackinnon, R. (1988) The structure of the potassium channel: molecular basis of K^+ conduction and selectivity, *Science 280*, 69−77.
3. Li-Smerin, Y., and Swartz, K. J. (1998) Gating modifier toxins reveal a conserved structural motif in voltage-gated Ca^{2+} and K^+ channels, *Proc. Natl. Acad. Sci. U.S.A. 95*, 8585−8589.
4. Li-Smerin, Y., Hackos, D. H., and Swartz, K. J. (2000) Alpha-helical structural elements within the voltage-sensing domains of a K^+ channel, *J. Gen. Physiol. 115*, 33−49.
5. Lu, Z., Klem, A. M., and Ramu, T. (2001) Ion conduction pore is conserved among potassium channels, *Nature 413*, 809−813.
6. Jiang, Y., Lee, A., Chen, J., Ruta, V., Cadene, M., Chait, B. T., and MacKinnon, R. (2003) X-ray structure of a voltage-dependent K^+ channel, *Nature 423*, 33−41.
7. French, R. J., and Dudley, S. C., Jr. (1999) Pore-blocking toxins as probes of voltage-dependent channels, *Methods Enzymol. 294*, 575−605.
8. Ott, K. H., Becker, S., Gordon, R. D., and Ruterjans, H. (1991) Solution structure of mu-conotoxin GIIIA analysed by 2D-NMR and distance geometry calculations, *FEBS Lett. 278*, 160−166.
9. Hill, J. M., Alewood, P. F., and Craik, D. J. (1996) Three-dimensional solution structure of mu-conotoxin GIIIB, a specific blocker of skeletal muscle sodium channels, *Biochemistry 35*, 8824−8835.
10. Bontems, F., Roumestand, C., Gilquin, B., Menez, A., and Toma, F. (1991) Refined structure of charybdotoxin: common motifs in scorpion toxins and insect defensins, *Science 254*, 1521−1523.
11. Davis, J. H., Bradley, E. K., Miljanich, G. P., Nadasdi, L., Ramachandran, J., and Basus, V. J. (1993) Solution structure of omega-conotoxin GVIA using 2-D NMR spectroscopy and relaxation matrix analysis, *Biochemistry 32*, 7396−7405.
12. Kohno, T., Kim, J. I., Kobayashi, K., Kodera, Y., Maeda, T., and Sato, K. (1995) Three-dimensional structure in solution of the calcium channel blocker omega-conotoxin MVIIA, *Biochemistry 34*, 10256−10265.
13. Farr-Jones, S., Miljanich, G. P., Nadasdi, L., Ramachandran, J., and Basus, V. J. (1995) Solution structure of omega-conotoxin MVIIC, a high affinity ligand of P-type calcium channels, using ^1H NMR spectroscopy and complete relaxation matrix analysis, *J. Mol. Biol. 248*, 106−124.
14. Anderson, C. S., Makinnon, R., Smith, C., and Miller, C. (1988) Charybdotoxin block of single Ca^{2+}-activated K^+ channels. Effects of channel gating, voltage, and ion strength, *J. Gen. Physiol. 91*, 317−333.
15. Mackinnon, R., and Miller, C. (1988) Mechanism of charybdotoxin block of the high-conductance, Ca^{2+}-activated K^+ channel, *J. Gen. Physiol. 91*, 335−349.
16. Park, C. S., and Miller, C. (1992) Interaction of charybdotoxin with permeant ions inside the pore of a K^+ channel, *Neuron 9*, 307−313.

17. Cestele, S., and Catterall, W. A. (2000) Molecular mechanisms of neurotoxin action on voltage-gated sodium channels, *Biochimie 82*, 883−892.
18. Jablonsky, M. J., Watt, D. D., and Krishna, N. R. (1995) Solution structure of an Old World-like neurotoxin from the venom of the New World scorpion Centruroides sculpturatus Ewing, *J. Mol. Biol. 248*, 449−458.
19. Manoleras, N., and Norton, R. S. (1994) Three-dimensional structure in solution of neurotoxin III from the sea anemone *Anemonia sulcata*, *Biochemistry 33*, 11051−11061.
20. Kim, J. I., Konishi, S., Iwai, H., Kohno, T., Gouda, H., Shimada, I., Sato, K., and Arata, Y. (1995) Three-dimensional solution structure of the calcium channel antagonist omega-agatoxin IVA: consensus molecular folding of calcium channel blockers, *J. Mol. Biol. 250*, 659−671.
21. Takahashi, H., Kim, J. I., Min, H. J., Sato, K., Swartz, K. J., and Shimada, I. (2000) Solution structure of hanatoxin1, a gating modifier of voltage-dependent K(+) channels: common surface features of gating modifier toxins, *J. Mol. Biol. 297*, 771−780.
22. Takeuchi, K., Park, E., Lee, C., Kim, J. I., Takahashi, H., Swartz, K., and Shimada I. (2002) Solution structure of omega-grammotoxin SIA, a gating modifier of P/Q and N-type Ca(2+) channel, *J. Mol. Biol. 321*, 517−526.
23. Lee, C. W., Kim, S., Roh, S. H., Endoh, H., Kodera, Y., Maeda, T., Kohno, T., Wang, J. M., Swartz, K. J., and Kim, J. I. (2004) Solution structure and functional characterization of SGTx1, a modifier of Kv2.1 channel gating, *Biochemistry 43*, 890−897.
24. Ruta, V., Jiang, Y., Lee, A., Chen, J., and MacKinnon, R. (2003) Functional analysis of an archaebacterial voltage-dependent K^+ channel, *Nature 422*, 180−185.
25. Jiang, Y., Ruta, V., Chen, J., Lee, A., and MacKinnon, R. (2003) The principle of gating charge movement in a voltage-dependent K^+ channel, *Nature 423*, 42−48.
26. Swartz, K. J., and Mackinnon, R. (1997) Hanatoxin modifiers the gating of a voltage-dependent K^+ channel through multiple binding sites, *Neuron 18*, 665−673.
27. Swartz, K. J., and Mackinnon, R. (1997) Mapping the receptor site for hanatoxin, a gating modifier of voltage-dependent K^+ channels, *Neuron 18*, 675−682.
28. Li-Smerin, Y., and Swartz, K. J. (2000) Localization and molecular determinants of the Hanatoxin receptors on the voltage-sensing domains of a K(+) channel, *J. Gen. Physiol. 115*, 673−684.
29. Li-Smerin, Y., and Swartz, K. J. (2001) Helical structure of the COOH terminus of S3 and its contribution to the gating modifier toxin receptor in voltage-gated ion channels, *J. Gen. Physiol. 117*, 205−218.
30. Lee, S. Y., and MacKinnon, R. (2004) A membrane-access mechanism of ion channel inhibition by voltage sensor toxins from spider venom, *Nature 430*, 232−235.
31. Lee, H. C., Wang, J. M., and Swartz, K. J. (2003) Interaction between extracellular Hanatoxin and the resting conformation of the voltage-sensor paddle in Kv channels, *Neuron 40*, 527−536.
32. Wang, J. M., Roh, S. H., Kim, S., Lee, C. W., Kim, J. I., and Swartz, K. J. (2004) Molecular surface of tarantula toxins interacting with voltage sensors in K(v) channels, *J. Gen. Physiol. 123*, 455−467.
33. Bax, A., and Davis, D. G. (1985) MLEV-17-based two-dimensional homonuclear magnetization transfer spectroscopy, *J. Magn. Reson. 65*, 355−360.
34. Piotto, M., Saudek, V., and Sklenar, V. (1992) Gradient-tailored excitation for single-quantum NMR spectroscopy of aqueous solutions, *J. Biomol. NMR 2*, 661−665.
35. Rance, M., Sørensen, O. W., Bodenhausen, G., Wagner, G., Ernst, R. R., and Wüthrich, K. (1983) Improved spectral resolution in cosy ^{1}H NMR spectra of proteins via double quantum filtering, *Biochem. Biophys. Res. Commun. 117*, 479−485.
36. Mueller, L. (1987) P.E. COSY. a simple alternative to E. COSY, *J. Magn. Reson. 72*, 191−196.
37. Wüthrich, K., Billeter, M., and Braun, W. (1983) Pseudo-structures for the 20 common amino acids for use in studies of protein conformations by measurements of intramolecular proton-proton distance constraints with nuclear magnetic resonance, *J. Mol. Biol. 169*, 949−961.
38. Clore, M., Gronenborn, A. M., Nilges, M., and Ryan, C. A. (1987) Three-dimensional structure of potato carboxypeptidase inhibitor in solution. A study using nuclear magnetic resonance, distance geometry, and restrained molecular dynamics, *Biochemisty 26*, 8012−8023.
39. Pardi, A., Billeter, M., and Wuthrich K. (1984) Calibration of the angular dependence of the amide proton-C alpha proton coupling constants, $^3J_{HN}$ alpha, in a globular protein. Use of $^3J_{HN}$ alpha for identification of helical secondary structure, *J. Mol. Biol. 180*, 741−751.
40. Kline, A. D., Braun, W., and Wuthrich, K. (1988) Determination of the complete three-dimensional structure of the alpha-amylase inhibitor tendamistat in aqueous solution by nuclear magnetic resonance and distance geometry, *J. Mol. Biol. 204*, 675−724.
41. Hyberts, S. G., Marki, W., and Wagner, G. (1987) Stereospecific assignments of side-chain protons and characterization of torsion angles in Eglin c, *Eur. J. Biochem. 164*, 625−635.
42. Wagner, G., Braun, W., Havel, T. F., Schaumann, T., Go, N., and Wuthrich, K. (1987) Protein structures in solution by nuclear magnetic resonance and distance geometry. The polypeptide fold of the basic pancreatic trypsin inhibitor determined using two different algorithms, DISGEO and DISMAN, *J. Mol. Biol. 196*, 611−639.
43. Fletcher, J. I., Chapman, B. E., Mackay, J. P., Howden, M. E., and King, G. F. (1997) The structure of versutoxin (delta-atracotoxin-Hv1) provides insights into the binding of site 3 neurotoxins to the voltage-gated sodium channel, *Structure 5*, 1525−1535.
44. Nilges, M. (1995) Calculation of protein structures with ambiguous distance restraints. Automated assignment of ambiguous NOE cross-peaks and disulphide connectivities, *J. Mol. Biol. 245*, 645−660.
45. Laskowski, R. A., Rullmannn, J. A., MacArthur, M. W., Kaptein, R., and Thornton, J. M. (1996) AQUA and PROCHECK-NMR: programs for checking the quality of protein structures solved by NMR, *J. Biomol. NMR 8*, 477−486.
46. Koradi, R., Billeter, M., and Wüthrich, K. (1996) MOLMOL: a program for display and analysis of macromolecular structures, *J. Mol. Graph*ics *14*, 29−32.
47. Brünger, A. T. (1992) *X-PLOR Manual*, Version 3.1, Yale University, New Haven, CT.
48. Song, Y. M., Yang, S. T., Lim, S. S., Kim, Y., Hahm, K. S., Kim, J. I., and Shin, S. Y. (2004) Effects of L- or D-Pro incorporation into hydrophobic or hydrophilic helix face of amphipathic alpha-helical model peptide on structure and cell selectivity, *Biochem. Biophys. Res. Commun. 314*, 615−621.
49. Wüthrich, K. (1986) *NMR of Protein and Nucleic Acids*, John Wiley and Sons, New York.
50. Wimley, W. C., and White, S. H. (1993) Quantitation of electrostatic and hydrophobic membrane interactions by equilibrium dialysis and reverse-phase HPLC, *Anal. Biochem. 213*, 213−217.
51. Lakowicz, J. R. (1999) *Principles of Fluorescence Spectroscopy*, 2nd ed., p 698, Kluwer Academic/Plenum, New York.
52. Ghosh, A. K., Rukmini, R., and Chattopadhyay, A. (1997) Modulation of tryptophan environment in membrane-bound melittin by negatively charged phospholipids: implications in membrane organization and function, *Biochemistry 36*, 14291−14305.
53. Suchyna, T. M., Johnson, J. H., Hamer, K., Leykam, J. F., Gage, D. A., Clemo, H. F., Baumgarten, C. M., and Sachs, F. (2000) Identification of a peptide toxin from *Grammostola spatulata* spider venom that blocks cation-selective stretch-activated channels, *J. Gen. Physiol. 115*, 583−598.
54. Suchyna, T. M., Tape, S. E., Koeppe, R. E., II, Andersen, O. S., Sachs, F., and Gottlieb, P. A. (2004) Bilayer-dependent inhibition of mechanosensitive channels by neuroactive peptide enantiomers, *Nature 430*, 235−240.
55. Murray, D., Arbuzova, A., Hangyas-Mihalyne, G., Gambhir, A., Ben-Tal, N., Honig, B., and McLaughlin, S. (1999) Electrostatic properties of membranes containing acidic lipids and adsorbed basic peptides: theory and experiment, *Biophys J. 77*, 3176−3188.
56. Ruta, V., and MacKinnon, R. (2004) Localization of the voltage-sensor toxin receptor on KvAP, *Biochemistry 43*, 10071−10079.

BI0477034